RESEARCH ARTICLE

JENER Journal of Empirical and Non-Empirical Research
Volume 2, Issue 2, Page 354-366 | Article No. 42
DOI: 10.4898/jener.v2i2.a42
ISSN: 7895-9216
Journal homepage: https://jenerjournal.com
Journal email: editor@jenerjournal.com

JENER Journal
JENER Journal of Empirical and Non-Empirical Research

Steady Casson Fluid Flow over an Exponentially Stretching Sheet: Heat and Mass Transfer with Arrhenius Chemical Reaction

Apelebiri Theophilus[1], Okwoli Christian[2], Anyanwu Emeka[3], Olanrewaju Philip Oladapo[4]

[1,2,3,4]Department of Mathematics, Federal University Wukari, Nigeria

ARTICLE INFORMATION

Article history:
Published: February 2026

Keywords:
Steady Casson Fluid Flow
Exponentially Stretching Sheet
Heat and Mass Transfer
Arrhenius Chemical Reaction

ABSTRACT

This study investigates steady two-dimensional boundary layer flow, heat and mass transfer of a Casson fluid over an exponentially stretching sheet in the presence of an Arrhenius chemical reaction. The governing nonlinear partial differential equations describing momentum, energy, and species concentration are formulated by employing suitable similarity transformations, the system is reduced to a coupled set of nonlinear ordinary differential equations, which are solved numerically using shooting technique in conjunction with Runge-Kutta scheme. The effects of key physical parameters, including the Casson fluid parameter, reaction rate constant, activation energy, Prandtl number, and Schmidt number, on velocity, temperature, and concentration distributions are examined. The corresponding variations in skin friction coefficient, Nusselt number and Sherwood number are analyzed. The results reveal that increasing the Casson parameter suppresses the fluid velocity while enhancing thermal and concentration boundary layer thickness. Higher activation energy weakens the chemical reaction rate, leading to an increase in species concentration near the sheet.

1. Introduction

Boundary layer flow which is being induced by stretching surfaces is of great interest because of its relevance to polymer processing, extrusion, wire drawing, coating and related manufacturing operations. Such processes which involve the transport of momentum, heat and mass within the boundary layer governs the product quality especially during heating, cooling and chemical treatment stages. Likewise, classical analyses were restricted to Newtonian fluids and linearly stretching sheets in which many practical systems involving non-Newtonian behaviour and nonlinear stretching rates which modify the flow structure.

The Casson fluid model provides an appropriate framework for the description of yield stress materials that behave as rigid bodies below a critical shear stress which also exhibit shear thinning characteristics once motion commences. This model has been found very useful in food engineering, coating technologies and hemodynamics where it is usually deployed to approximate blood flow at low shear rates. The presence of yield stress always changes the velocity distribution, wall shear stress, heat and concentration boundary layers.

Exponentially stretching surfaces constitute a distinct class of problems in which the stretching rate intensifies along the sheet thereby leading to notable variations in boundary layer thickness and transport rates compared with linear stretching cases. When heat and mass transfer are coupled with Arrhenius chemical reactions the resulting system becomes strongly nonlinear due to the temperature dependent reaction rate.

The present study examines the steady boundary layer flow of a Casson fluid over an exponentially stretching sheet with heat and mass transfer in the presence of an Arrhenius chemical reaction. Emphasis is placed on the influence of thermal and reaction parameters on the velocity, temperature and concentration fields as well as on quantities of engineering interest.

2. Literature Review

The role of non-Newtonian fluids in fluid mechanics cannot be overemphasized due to their various involvement in industrial processes as well as biological systems. Unlike other fluids, they usually display a nonlinear relationship between shear stress and shear rate which has led to the development of various models such as the Jeffrey, elastic, micropolar, and Casson fluid models. Amidst these models, the Casson model has been of interest because of its effectiveness in representing yield-stress property fluids (Ali et al., 2020).

A Casson fluid has a distinguishing yield stress that when applied the shear stress is below threshold such material behaves as a rigid body and once the threshold is exceeded flow starts and the fluid usually displays shear-thinning property. The viscosity increases as the shear rate rises to zero and decreases as well at high shear rates (Ali et al., 2020). These properties qualify the Casson model to display solid-like resistance and fluid-like motion. (Elgendi et al., 2024; Khader & Babatin, 2023).

Casson fluids are useful in a variety of engineering and industrial applications such as food processing and coating technologies. Typical good examples of Casson fluids include honey, ketchup, paints, shampoos, tomato products, and concentrated fruit juices (Ali et al., 2020). One of the major applications of the Casson fluids model can be seen in biomedical fluid mechanics in which it has been widely deployed to describe blood flow under low shear conditions (Ali et al., 2020; Fatahian et al., 2018).

Researchers have shown that at low shear rates red blood cells form rouleaux structures which leads to increased effective viscosity and velocity profiles that deviate from the classical parabolic distribution (Panigrahi et al., 2020). Moreso, it is noted that the yield stress of normal human blood lies in the range 0.01–0.06 dyn/cm² which confirms its weakness but not negligible yield stress nature (Deepthi & Rallabandi, 2023). These observations define the reason for the continued use of the Casson fluid model in analytical and computational studies of blood flow under physiological and pathological conditions (Fatahian et al., 2018; Panigrahi et al., 2020).

The boundary layer flow which are generated by stretching surfaces bring about a topic of interest in fluid dynamics because it gives birth to many industrial manufacturing processes. For example, the stretching velocity may vary linearly follow a power-law or increase exponentially along the surface such configurations are of importance in polymer extrusion, hot rolling, glass blowing, continuous casting, wire drawing, paper production, crystal growth, cable coating, and metal spinning (Asghar et al., 2015; Bognár, 2016; Bognar & Hriczo, 2020; Khan et al., 2015; Rao, 2018; Shaheen et al., 2019; Singh et al., 2019). The boundary layer structure and heat transfer are of great influence in bringing about product quality in all of these applications especially during heating and cooling stages (Khan et al., 2015; Veerabhadrappa et al., 2020).

The theoretical background for stretching sheet boundary layer flows is believed to have originated from the pioneering studies of Sakiadis and Crane. Sakiadis first analyzed boundary layer flow over a continuously moving surface which is extended to classical boundary layer theory to like surface motion (Hussain et al., 2022; Mustafa et al., 2013; Singh et al., 2019). Crane subsequently worked on an exact analytical solution for laminar flow which is induced by a linearly stretching sheet which has a long serving as a benchmark for numerous investigations (Bognar & Hriczo, 2020; Hussain et al., 2022; Mustafa et al., 2013; Singh et al., 2019). Many of these researchers were motivated by polymer sheet processing which has established a framework that is widely extended to incorporate non-Newtonian rheology as well as transport phenomena.

Further research has investigated boundary layer flows over stretching surfaces in the presence of heat and mass transfer, magnetic fields, porous media, viscoelastic effects, and chemical reactions (Bég et al., 2013; Mustafa et al., 2013). Among this broad class of problems exponentially stretching surfaces has constituted a distinct and important category. Magyari and Keller were among the first to develop similarity solutions for flow and thermal boundary layers over exponentially stretching sheets demonstrating how exponential stretching can modify boundary layer behaviour in relation to linear or power-law cases (Beg et al., 2013; Sharada & Shankar, 2015; Veerabhadrappa et al., 2020).

In this research we investigate the steady boundary layer flow of a Casson fluid over an exponentially stretching sheet incorporating coupled heat, mass transfer and an Arrhenius chemical reaction. The effects of key thermal, and concentration parameters on the velocity, temperature, and concentration fields as well as on relevant engineering quantities are analyzed. The results are aimed to enhance the understanding of transport processes in yield stress non-Newtonian fluids which can provide vital insights that are relevant to industrial and biomedical applications involving exponentially stretching surfaces.

3. Mathematical Analysis

We analyze the extension of an expanding exterior with a 2D flow of incompressible, viscous conducting electricity magnetohydrodynamic (MHD) Casson fluid. The flow is restricted to $y>0$ A variable attractive medium $B=B_0\exp^{\frac{x}{2L}}$ is practical regular to the piece. The expanding flow $U=U_0\exp^{x/L}$, thermal spread $T_w=T_\infty+T_0\exp^{x/L}$. In addition to attentiveness $C_w=C_\infty+C_0\exp^{x/L}$ The surface is stretched along the axis by two opposing forces as well as equal forces while the sources remain permanent with a thin piece exerting beginning a narrow opening. A.S. Rao et al (2025). The equations that govern this flow can be written as:

Continuity Equation

$$\frac{\partial u}{\partial x}+\frac{\partial v}{\partial y}=0 \tag{1}$$

Momentum Equation

$$u\frac{\partial u}{\partial x}+v\frac{\partial u}{\partial y}=\upsilon\left(1+\frac{1}{\rho}\right)\left(\frac{\partial^2 u}{\partial x^2}+\frac{\partial^2 u}{\partial y^2}\right)g\beta_T\left(T-T_\infty\right)+g\beta_c\left(C-C_\infty\right)-\frac{\delta B_0^2 u}{\rho} \tag{2}$$

Energy Equation

$$u\frac{\partial T}{\partial x}+v\frac{\partial T}{\partial y}=\frac{k}{\ell c\rho}\frac{\partial^2 T}{\partial y^2}-\frac{1}{(\ell c\rho)}\frac{\partial q_r}{\partial y}+\frac{1}{\ell c\rho S}Q_0\left(T-T_\infty\right)+\frac{\upsilon}{c\rho}\left(\frac{\partial u}{\partial y}\right)^2 \tag{3}$$

Concentration Equation

$$u\frac{\partial c}{\partial x}+v\frac{\partial c}{\partial y}=D_B\frac{\partial^2 c}{\partial y^2}-k_r^2\left(\frac{T}{T_\infty}\right)\exp\left(\frac{-E_a}{kT}\right)\left(c-c_\infty\right) \tag{4}$$

Satisfy the border circumstances/conditions

$$u = U + N\mu\frac{\partial u}{\partial y}, v = -V(x), T = T_w + m\frac{\partial T}{\partial y}, c = cw + \rho\frac{\partial c}{\partial y} \quad \text{at y = 0} \qquad (5)$$

$$u \to 0, T \to T_\infty, c \to c_\infty \text{ as } y \to \infty \qquad (6)$$

Where u and v are the velocities, v is the kinematic viscosity

Assessing the electromagnetic temperature flow using the Rosseland estimate q_r provides by

$$q_r = -\frac{4\delta^*}{3x^*}\frac{\partial T^4}{\partial y} = -\frac{16\delta^* T_\infty^3}{3(\ell c\rho)k^*}\frac{\partial^2 T}{\partial y^{2s}} \qquad (7)$$

Since $T^4 \cong 4T_\infty^3 T - 3T_\infty^4$

3.1 Solution by similarity variables

The PDEs in (1)–(4) were transformed to ODEs by use of similarity variables. Using the following transformation, we obtain non-dimensionalisation of (1)-(4):

$$\eta = \left(\frac{U_0}{2\upsilon L}\right)^{1/2}\exp^{x/2L} y, \quad u = U_0\exp^{x/L} f', \quad v = -\left(\frac{\upsilon U_0}{2\upsilon L}\right)^{1/2}\exp^{x/2L}\left[f - \eta f'\right], \quad \psi = \left(2L\upsilon U_0\right)^{1/2}\exp^{1/2L} f,$$

$$\theta = \frac{T - T_0}{T_f - T_\infty}, \quad \phi = \frac{c - c_\infty}{c_w - c_\infty} \qquad (8)$$

Utilizing the stream, function $u = \frac{\partial\psi}{\partial y}, v = -\frac{\partial\psi}{\partial x}$ (9)

ψ is the stream function while the Cauchy-Riemann equations are: $u = \frac{\partial\psi}{\partial y}, v = -\frac{\partial\psi}{\partial x}$

Substituting (9) into (1) we have:

$$\frac{\partial u}{\partial x} + \frac{\partial v}{\partial y} = \frac{\partial}{\partial x}\left(\frac{\partial\psi}{\partial y}\right) + \frac{\partial}{\partial y}\left(-\frac{\partial\psi}{\partial x}\right)$$

$$= \frac{\partial^2\psi}{\partial x\partial y} - \frac{\partial^2\psi}{\partial y\partial x}$$

$$= \frac{\partial^2\psi}{\partial x\partial y} - \frac{\partial^2\psi}{\partial x\partial y} = 0$$

$$\frac{\partial u}{\partial x} + \frac{\partial v}{\partial y} = 0$$

Thus (Satisfied)

Substituting equation (8) into (2) - (4) gives:

$$\left(1 + \frac{1}{\beta}\right)f''' - 2f'^2 + ff'' + G_{T_x}\theta + G_{c_x}\phi - Mf' = 0 \qquad (10)$$

$$\left(1 + \frac{4Ra}{3}\right)\theta'' + \Pr\theta' f - \Pr\theta f' + \lambda\Pr\theta + \Pr Ecf''^2 = 0 \qquad (11)$$

$$\phi'' + Sc\left(f\phi' - f'\phi\right) - ScY\left(1 + \eta\theta_w\theta\right)\exp\left(\frac{-E}{1 + \theta_w\theta}\right)\phi = 0 \qquad (12)$$

$$G_{T_x} = \frac{2Lg\beta_T\left(T_f - T_\infty\right)}{U_0^2\exp\left(\frac{2x}{L}\right)}$$

Where (Local thermal Grashof number)

$$G_{C_x} = \frac{2Lg\beta_c\left(c_w - c_\infty\right)}{U_0^2\exp\left(\frac{2x}{L}\right)}$$

(Local solutal Grashof number)

$M = 2L\frac{\delta\beta_0^2}{\rho U_0}$ (Magnetic field parameter)

$$Ra = \frac{4\delta * T_\infty^3}{k^* k}, \qquad Ec = \frac{LU_0^2}{cp\left(T_f - T_\infty\right)}, \quad \Pr = \frac{\upsilon}{\alpha}.$$

$$Sc = \frac{D_B}{\upsilon}, \quad \theta_w = \frac{\left(T_f - T_\infty\right)}{T_\infty}, \quad E = \frac{Ea}{kT_\infty}, \quad \gamma = \frac{2Lk_0^2}{U_0}$$

Satisfying the following conditions:

$$f(0) = S, f'(0) = 1 + S_v f''(0), \theta(0) = 1 + S_t\theta'(0), \phi(0) = 1 + S_c\phi'(0)$$
$$f'(\infty) = 0, \ \theta(\infty) = 0, \ \phi(\infty) = 0 \qquad (13)$$

Equation (10) -(12) along with (13) were solved in Maple 2025 using Runge-Kutta of order four for accuracy.

3.2 Computational procedure

The coupled equations (10) – (12) and the boundary conditions (13) were solved using the shooting approach and the Runge–Kutta method of order four. moreso, a numerical code was created and executed on the computer using MAPLE 2025 software. In order to verify the approach employed in the study, the acquired findings were compared with the available literature.

4. Results and Discussion

Table and graphs for embedded fluid flow parameters for better understanding of the flow model.

In table 4.1 the following parameters were kept fixed in order to note the influence of the new embedded flow values that are introduced as;

$M = 0.5$, $Ra = \lambda = S_V = S_t = S_c = 0.1$, $\Pr = 0.71$, $Sc = 0.60$, $\gamma = 0.2$

and it was established that thermal Grashof number Gr, solutal Grashof number Gc and the activation energy E brought a decrease in the wall temperature at larger values while Eckert number Ec, power exponent n and the relative temperature θ_w brought an increase in the wall initial temperature at bigger values while Eckert number Ec, power exponent n and the relative temperature θ_w brought a decrease to the wall initial temperature.

It is observed that increase in the thermal Grashof number Gr, solutal Grashof number Gc and the activation energy E reduces the skin friction coefficient at larger values while Eckert number Ec, power exponent n and the relative temperature θ_w enhances the skin friction coefficient when the values are raised.

Similarly, increasing the thermal Grashof number Gr, solutal Grashof number Gc and the activation energy E enhances the heat transfer rate at the wall while Eckert number Ec, power exponent n and the relative temperature θ_w reduces the heat transfer rate at the wall surface. Finally, larger values of Grashof number Gr, solutal Grashof number Gc and the activation energy E enhances the mass transfer rate at the wall while Eckert number Ec, power exponent n and the relative temperature θ_w reduces the mass transfer rate at the wall surface call the Sherwood number.

4.1 Presentation of Results in Tables

Table 1: Computations showing the effect of the active parameters on the initial temperature, initial concentration Skin friction coefficient, Nusselt number and Sherwood number for $M = 0.5$, $Ra = \lambda = S_V = S_t = S_c = 0.1$, $\Pr = 0.71$, $Sc = 0.60$, $\gamma = 0.2$

Gr	Gc	Ec	N	θ_w	E	$\theta(0)$	$\phi(0)$	$-f''(0)$	$-\theta'(0)$	$-\phi'(0)$
0.5	0.5	0.2	1	0.1	0	0.92830717	0.76252204	1.03844453	0.716928221	0.716928221
1	0.5	0.2	1	0.1	0	0.92571237	0.77638570	0.92620121	0.742876293	0.742876293
2	0.5	0.2	1	0.1	0	0.92175481	0.79511383	0.71738443	0.782451858	0.782451858
0.5	1	0.2	1	0.1	0	0.926431653	0.772546094	0.9513486595	0.735683469	0.735683469
0.5	2	0.2	1	0.1	0	0.9231955308	0.788349372	0.778812944	0.7680446912	0.7680446912
0.5	3	0.2	1	0.1	0	0.9204920898	0.800010345	0.609311237	0.795079101	0.795079101

0.5	0.5	0.4	1	0.1	0	0.933162841	0.710890344	1.041392495	0.6683715812	0.668371581
0.5	0.5	0.6	1	0.1	0	0.9380286836	0.659151918	1.044359922	0.6197131636	0.6197131636
0.5	0.5	1	1	0.1	0	0.9477934936	0.555324145	1.050355484	0.5220650639	0.5220650639
0.5	0.5	0.2	3	0.1	0	0.9283388045	0.754968051	1.039587014	0.7166119547	0.7166119547
0.5	0.5	0.2	5	0.1	0	0.9283696701	0.747597175	1.040701191	0.7163032980	0.7163032980
0.5	0.5	0.2	8	0.1	0	0.9284145945	0.736870258	1.042321509	0.7158540546	0.7158540546
0.5	0.5	0.2		0.3	0	0.9283388045	0.754968051	1.039587014	0.7166119547	0.7166119547
0.5	0.5	0.2		0.5	0	0.9283696701	0.747597175	1.040701191	0.7163032980	0.7163032980
0.5	0.5	0.2		0.7	0	0.9283997990	0.740403005	1.041788039	0.7160020090	0.7160020090
0.5	0.5	0.2		0.1	0.3	0.9282082753	0.780017045	1.035457330	0.7179172465	0.7179172465
0.5	0.5	0.2		0.1	0.5	0.9281525923	0.789762053	1.033785003	0.7184740766	0.7184740766
0.5	0.5	0.2		0.1	0.7	0.9281044121	0.798141535	1.032342675	0.7189558782	0.7189558782

4.2 Graphs Presentation

Figures 3.1-3.2 discussed the influence of Casson parameter β on the fluid velocity and temperature profiles. It was observed that increasing the Casson parameter reduces the fluid flow velocity profile while it thickens the thermal boundary layer profile. Figures 3.3-3.5 examined the effects of thermal Grashof number Gr on the fluid flow velocity, temperature and concentration distributions across the channel. When this parameter is raised, the fluid flow velocity profile thickened across the channel while the thermal boundary layer thickness and concentration boundary layer decreases. Similarly, the same effect was observed when the solutal Grashof number Gc was raised in Figures 3.6-3.8.

Figure 3.9 depicts the effects of magnetic field parameter on the velocity profile and it was seen that the higher the parameter the thinner the velocity profile because of the restriction on the flow due to the parameter while it enhances the thermal boundary layer thickness in Figure 3.10. Figures 3.11 and 3.12 discusses the influence of thermal radiation parameter Ra on the temperature and concentration distribution across the channel. Bigger values of thermal radiation parameter thickened the thermal boundary layer thickness and thinned the concentration profile. It can be seen in Figure 3.13 and 3.14 that larger value of Prandtl number $\Pr$ decreases the thermal boundary layer thickness and enhances the concentration boundary layer thickness.

The effects of internal heat generation λ on velocity, temperature and concentration distribution was plotted in Figures 3.15-3.17. Increasing the internal heat generation parameter thickened the velocity and thermal boundary layer thickness while it thinned the concentration distribution across the wall surfaces.

Figures 3.18 and 3.19 depicts the effects of Eckert number Ec on the temperature and concentration distribution. When Eckert number was increased, the thermal boundary layer thickness thickens while the concentration profile decreases across the wall surface.

Figures 3.20 – 3.23 depict the influence of Schmidt number Sc, chemical reaction parameter γ, relative temperature θ_w and activation energy parameter E on the concentration distribution and the larger values of the above parameters decreases the concentration boundary layer thickness across the wall surface.

Figure 3.24 represents the influence of initial flow velocity S on the velocity profiles and its reduces the velocity boundary layer thickness at a larger value. In Figure 3.25, as flow rate parameter increases, the velocity distribution thickened close to the wall surface. Figure 3.26 depicts the effect of flow heating slap on the temperature distribution and at greater values of this parameter reduces the thermal boundary layer thickness. Effects of flow heating slap on concentration profile in Figure 3.27 and it enhances the concentration distribution. The effects of solutal slide constraints parameter on concentration profile was plotted in Figure 3.28 and the bigger the values, the thicker the concentration profile while the order of chemical reaction effects on the concentration profile. It was observed that the higher the value of this order the thinner the concentration profile across the wall surface.

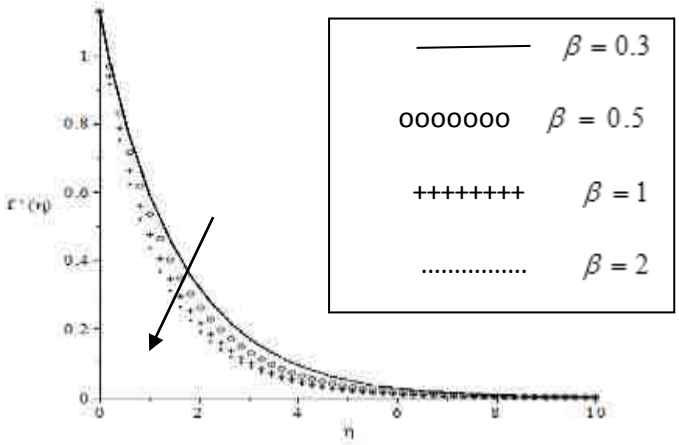

Figure 3.1: Effects of Casson fluid parameter β on the velocity profile with fix parameters values of $Gr = Gc = M = 0.5$, $\Pr = 0.71$, $Sc = 0.6$, $\gamma = Ec = 0.2$, $S = Ra = \lambda = S_V = S_t = S_c = \theta_w = E = 0.1$, $n = 1$

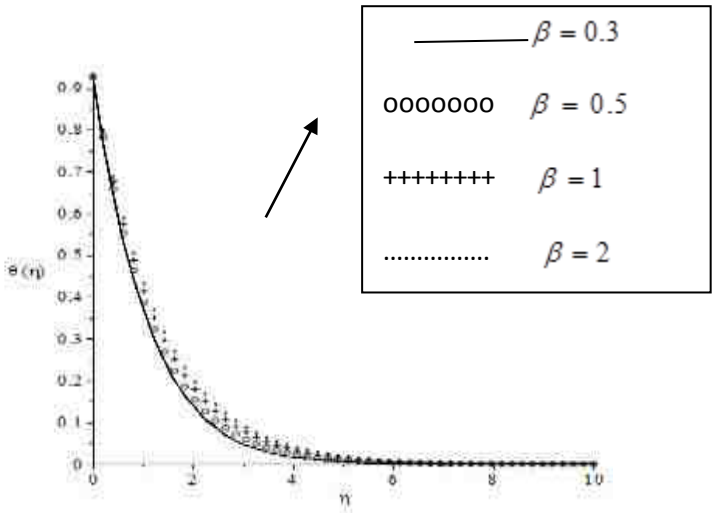

Figure 3.2: Effects of Casson fluid parameter β on the temperature distribution with fix parameters values of

$Gr = Gc = M = 0.5$, $\Pr = 0.71$, $Sc = 0.6$, $\gamma = Ec = 0.2$, $S = Ra = \lambda = S_V = S_t = S_c = \theta_w = E = 0.1$, $n = 1$

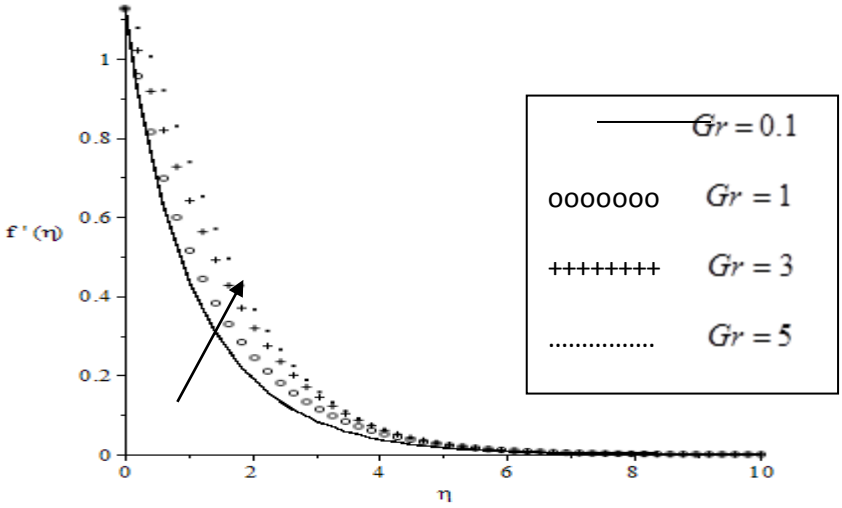

Figure 3.3: Effects of thermal Grashof number Gr on the velocity profile with fix parameters values of $Gc = M = 0.5, \Pr = 0.71, Sc = 0.6, \gamma = Ec = 0.2, S = Ra = \lambda = S_v = S_t = S_c = \theta_w = E = 0.1, n = 1, \beta = 1$

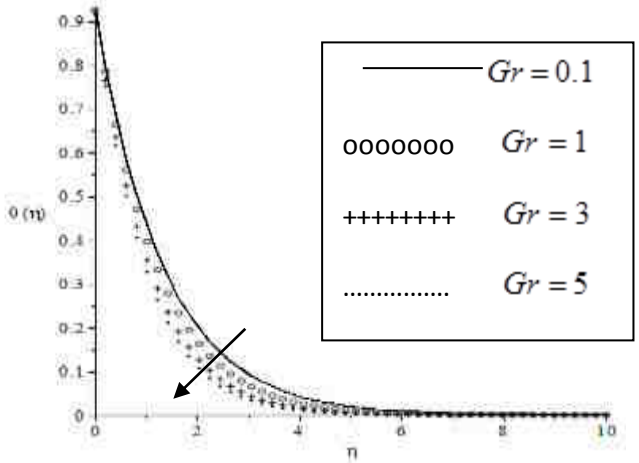

Figure 3.4: Effects of thermal Grashof number Gr on the temperature profile with fix parameters values of $Gc = M = 0.5$, $Gr = 5$, $Sc = 0.6$, $\gamma = Ec = 0.2$, $S = Ra = \lambda = S_V = S_t = S_c = \theta_w = E = 0.1$, $n = 1$, $b = 1$

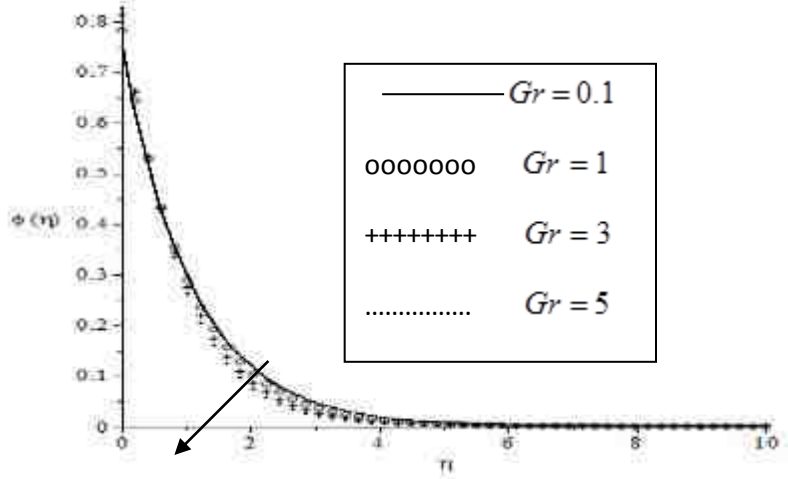

Figure 3.5: Effects of thermal Grashof number Gr on the concentration profile with fix parameters values of $Gc = M = 0.5$, $Gr = 5$, $Sc = 0.6$, $\gamma = Ec = 0.2$, $S = Ra = \lambda = S_V = S_t = S_c = \theta_w = E = 0.1$, $n = 1$, $b = 1$

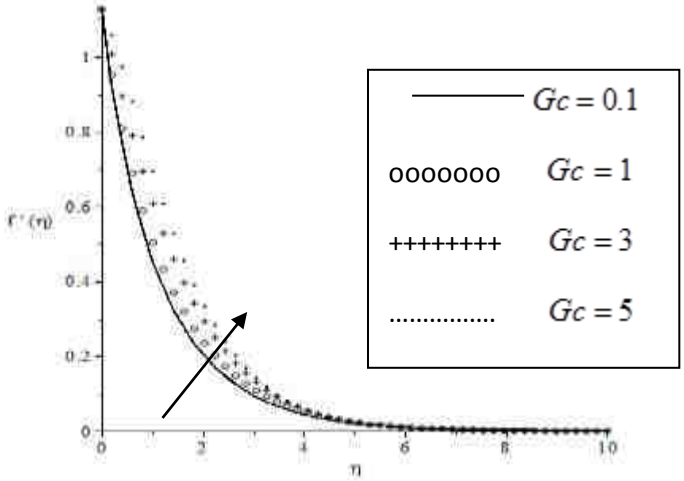

Figure 3.6: Effects of solutal Grashof number Gc on the velocity profile with fix parameters values of $Gr = M = 0.5$, $Gr = 5$, $Sc = 0.6$, $\gamma = Ec = 0.2$, $S = Ra = \lambda = S_V = S_t = S_c = \theta_w = E = 0.1$, $n = 1$, $b = 1$

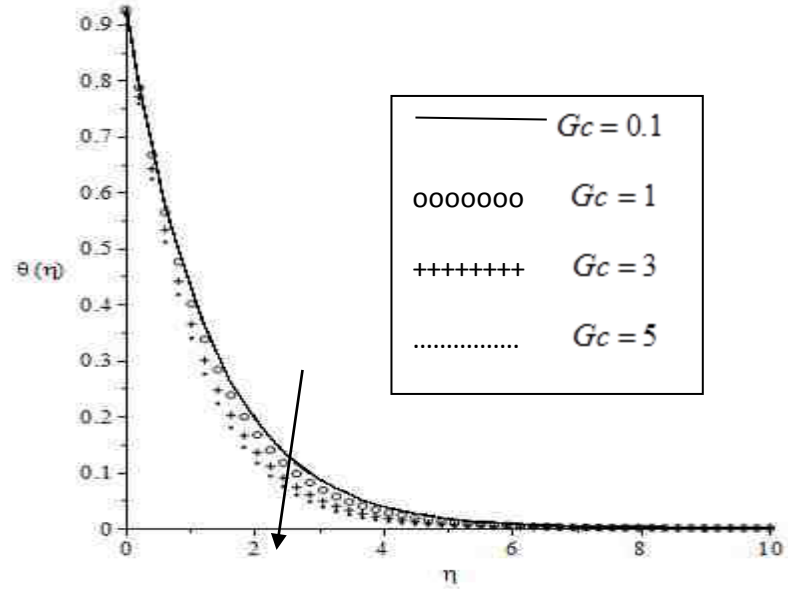

Figure 3.7: Effects of solutal Grashof number Gc on the temperature profile with fix parameters values of $Gr = M = 0.5$, $Gr = 5$, $Sc = 0.6$, $\gamma = Ec = 0.2$, $S = Ra = \lambda = S_V = S_t = S_c = \theta_w = E = 0.1$, $n = 1$, $b = 1$

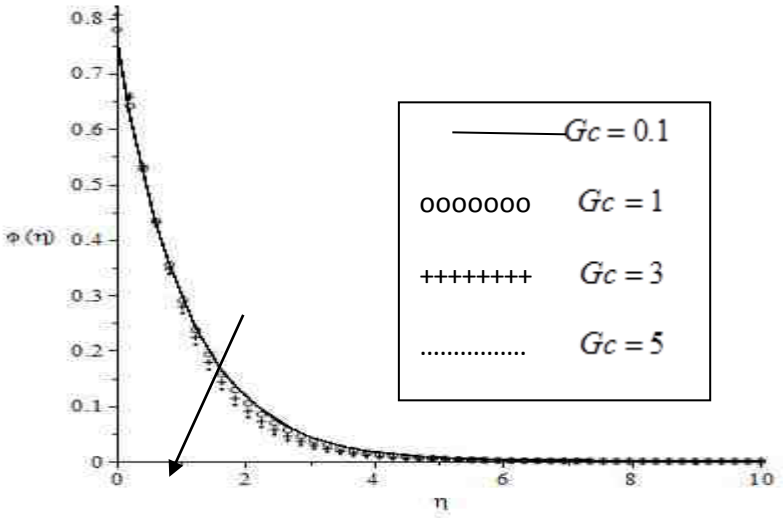

Figure 3.8: Effects of solutal Grashof number Gc on the concentration profile with fix parameters values of $Gr = M = 0.5$, $Gr = 5$, $Sc = 0.6$, $\gamma = Ec = 0.2$, $S = Ra = \lambda = S_V = S_t = S_c = \theta_w = E = 0.1$, $n = 1$, $b = 1$

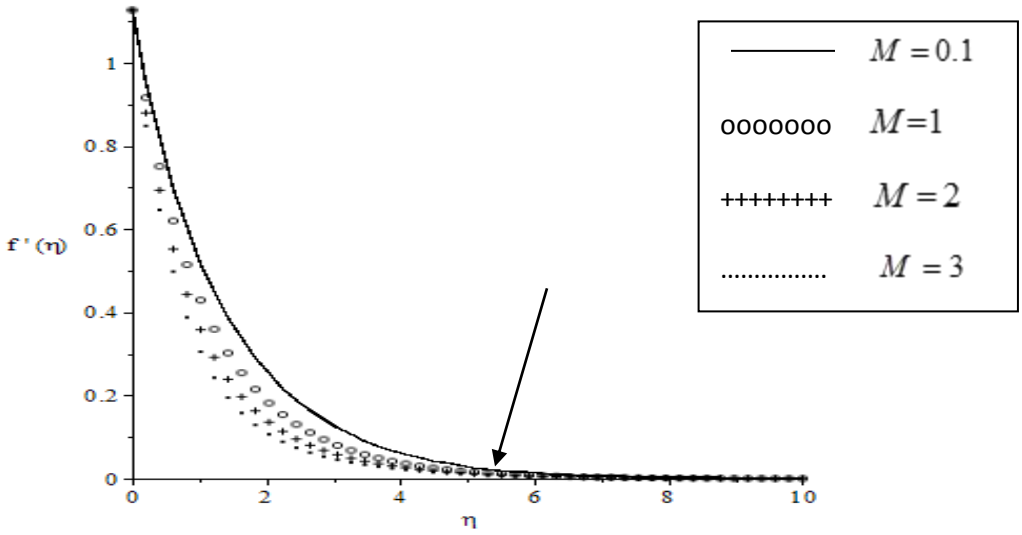

Figure 3.9: Effects of magnetic field parameter M on the velocity profile with fix parameters values of $Gr = Gc = 0.5$, $Gr = 5$, $Sc = 0.6$, $\gamma = Ec = 0.2$, $S = Ra = \lambda = S_V = S_t = S_c = \theta_w = E = 0.1$, $n = 1$, $b = 1$

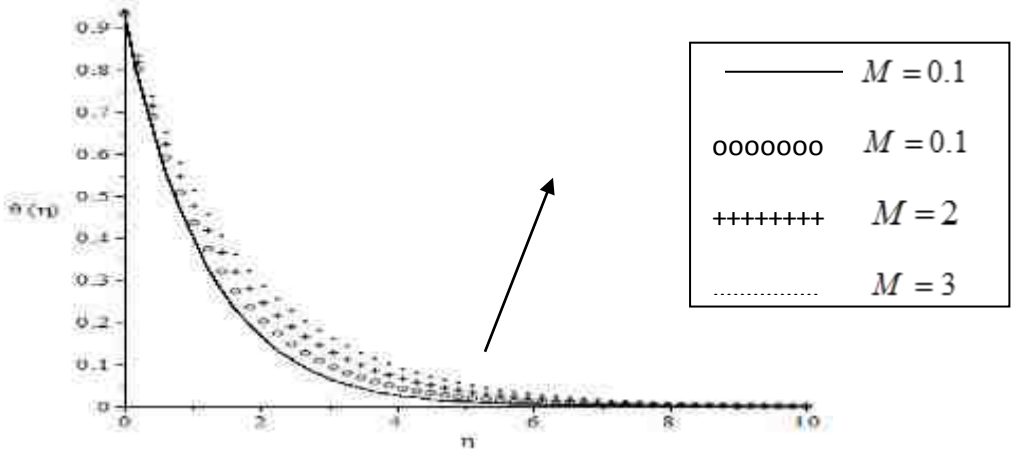

Figure 3.10: Effects of magnetic field parameter M on the temperature profile with fix parameters values of $Gr = Gc = 0.5$, $Gr = 5$, $Sc = 0.6$, $\gamma = Ec = 0.2$, $S = Ra = \lambda = S_V = S_t = S_c = \theta_w = E = 0.1$, $n = 1$, $b = 1$

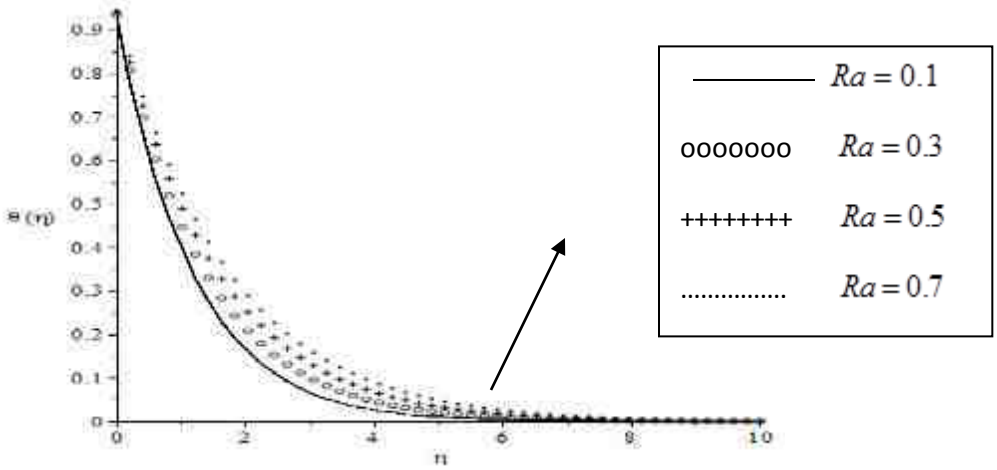

Figure 3.11: Effects of thermal radiation parameter Ra on the temperature profile with fix parameters values of $Gr = Gc = 0.5$, $Gr = 5$, $Sc = 0.6$, $\gamma = Ec = 0.2$, $S = Ra = \lambda = S_V = S_t = S_c = \theta_w = E = 0.1$, $n = 1$, $b = 1$

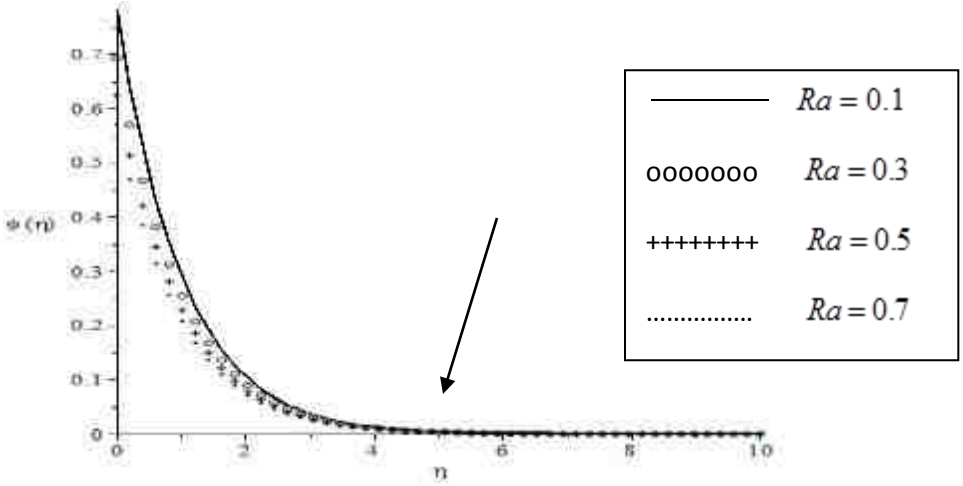

Figure 3.12: Effects of thermal radiation parameter Ra on the concentration profile with fix parameters values of $Gr = Gc = 0.5$, $Gr = 5$, $Sc = 0.6$, $\gamma = Ec = 0.2$, $S = Ra = \lambda = S_V = S_t = S_c = \theta_w = E = 0.1$, $n = 1$, $b = 1$

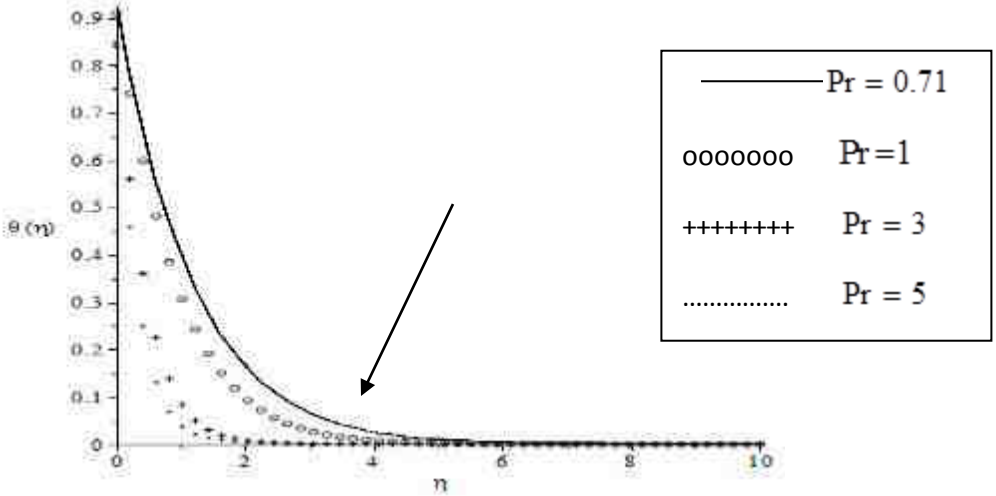

Figure 3.13: Effects of Prandtl number $\Pr$ on the temperature profile with fix parameters values of $Gr = Gc = 0.5$, $Sc = 0.6$, $\gamma = Ec = 0.2$, $S = M = \lambda = S_v = S_t = S_c = \theta_w = E = 0.1$, $n = 1$, $b = 1$, $Ra = 0.1$

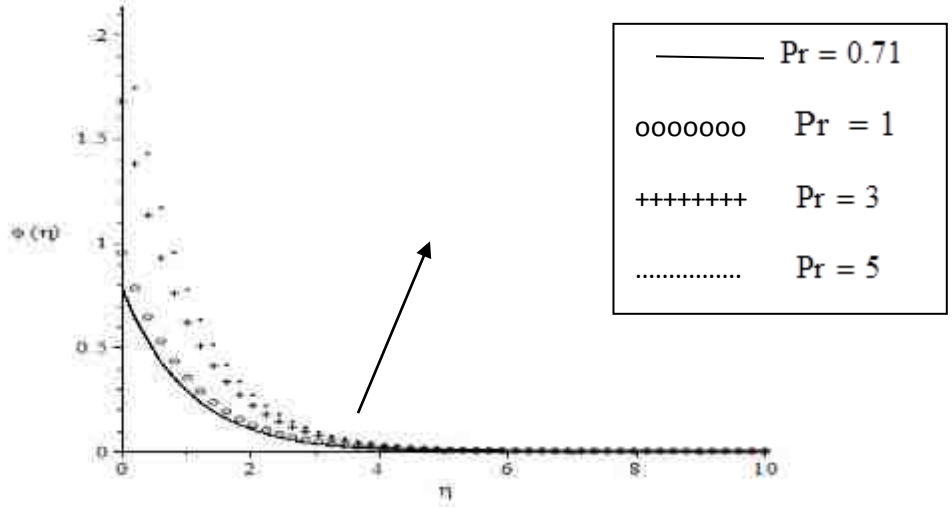

Figure 3.14: Effects of Prandtl number $\Pr$ on the concentration profile with fix parameters values of $Gr = Gc = 0.5$, $Sc = 0.6$, $\gamma = Ec = 0.2$, $S = M = \lambda = S_v = S_t = S_c = \theta_w = E = 0.1$, $n = 1$, $b = 1$, $Ra = 0.1$

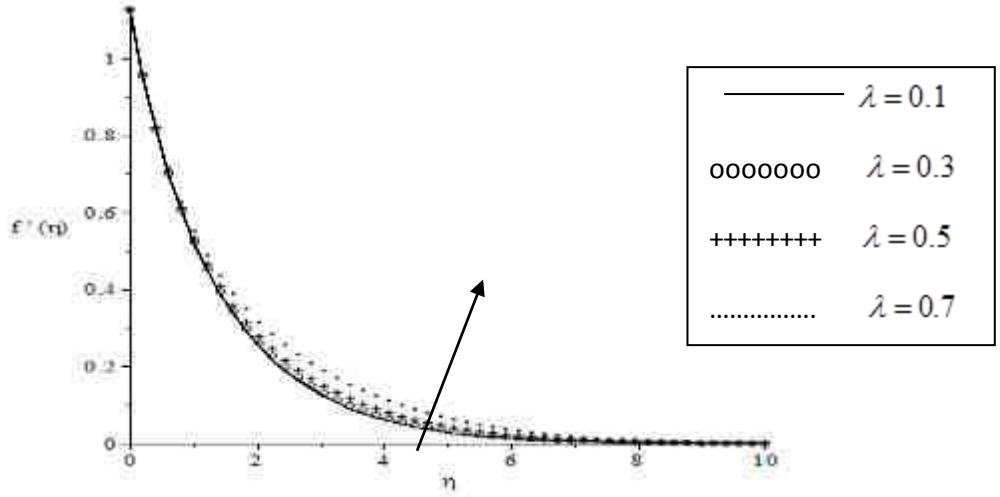

Figure 3.15: Effects of Internal heat generation parameter λ on the velocity profile with fix parameters values of $Gr = Gc = 0.5$, $Sc = 0.6$, $\gamma = Ec = 0.2$, $S = M = \lambda = S_v = S_t = S_c = \theta_w = E = 0.1$, $n = 1$, $b = 1$, $Ra = 0.1$, $\Pr = 0.71$

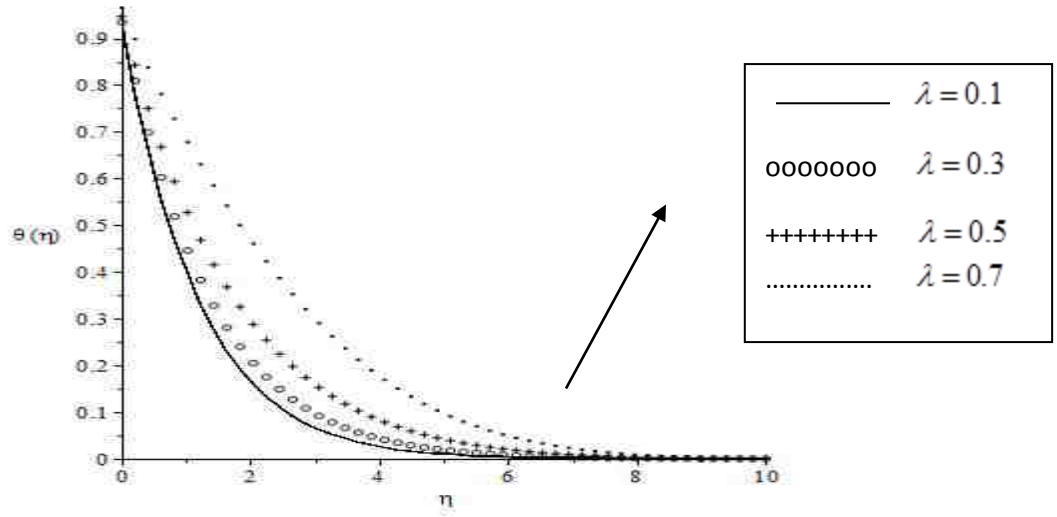

Figure 3.16: Effects of Internal heat generation parameter λ on the temperature profile with fix parameters values of $Gr = Gc = 0.5$, $Sc = 0.6$, $\gamma = Ec = 0.2$, $S = M = \lambda = S_v = S_t = S_c = \theta_w = E = 0.1$, $n = 1$, $b = 1$, $Ra = 0.1$, $\Pr = 0.71$

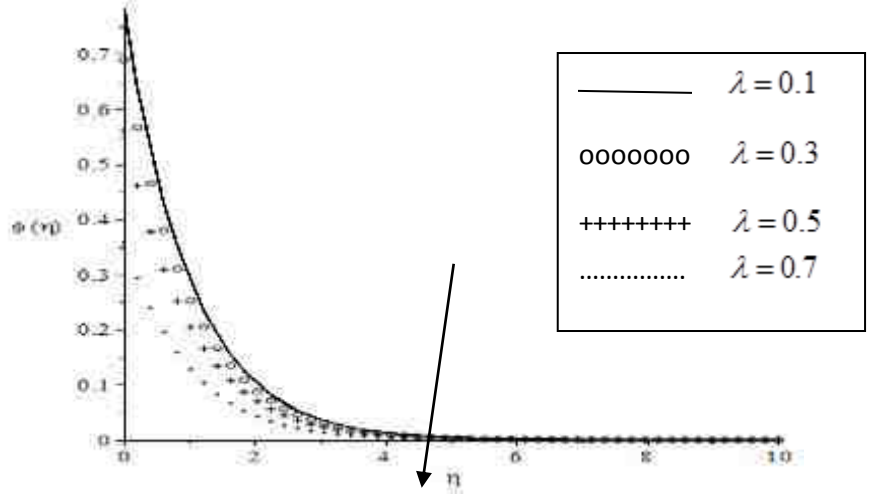

Figure 3.17: Effects of Internal heat generation parameter λ on the concentration profile with fix parameters values of $Gr = Gc = 0.5$, $Sc = 0.6$, $\gamma = Ec = 0.2$, $S = M = \lambda = S_v = S_t = S_c = \theta_w = E = 0.1$, $n = 1$, $b = 1$, $Ra = 0.1$, $\Pr = 0.71$

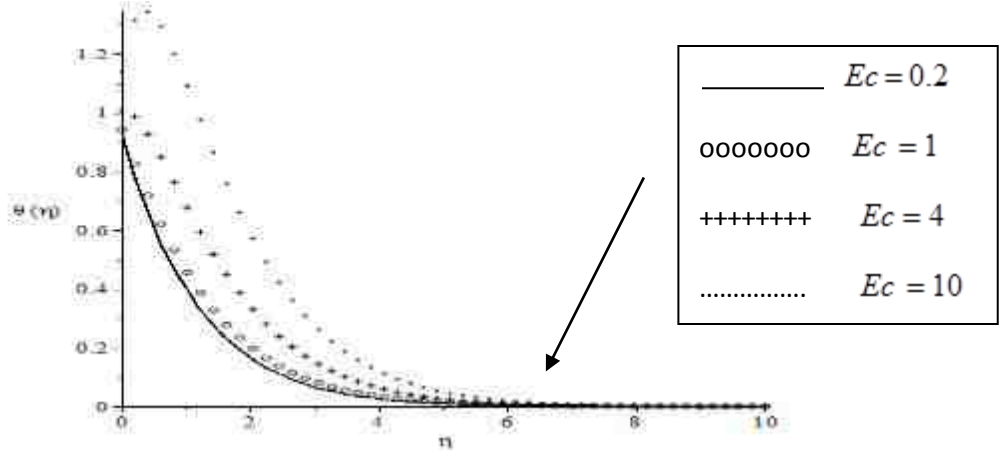

Figure 3.18: Effects of Eckert parameter Ec on the temperature profile with fix parameters values of $Gr = Gc = 0.5$, $Sc = 0.6$, $\gamma = 0.2$, $S = M = \lambda = S_v = S_t = S_c = \theta_w = E = 0.1$, $n = 1$, $b = 1$, $Ra = 0.1$, $\Pr = 0.71$, $\lambda = 0.1$

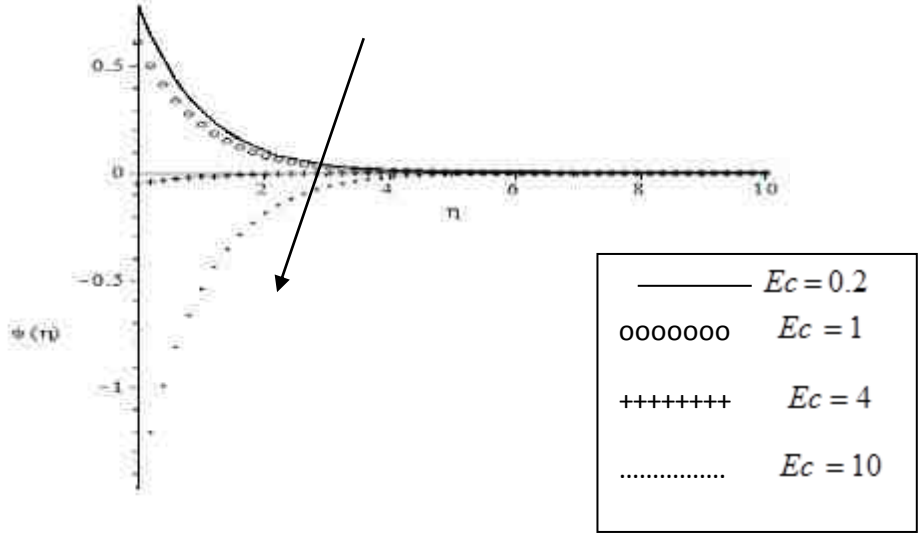

Figure 3.19: Effects of Eckert parameter Ec on the concentration profile with fix parameters values of $Gr = Gc = 0.5$, $Sc = 0.6$, $\gamma = 0.2$, $S = M = \lambda = S_v = S_t = S_c = \theta_w = E = 0.1$, $n = 1$, $b = 1$, $Ra = 0.1$, $\Pr = 0.71$, $\lambda = 0.1$

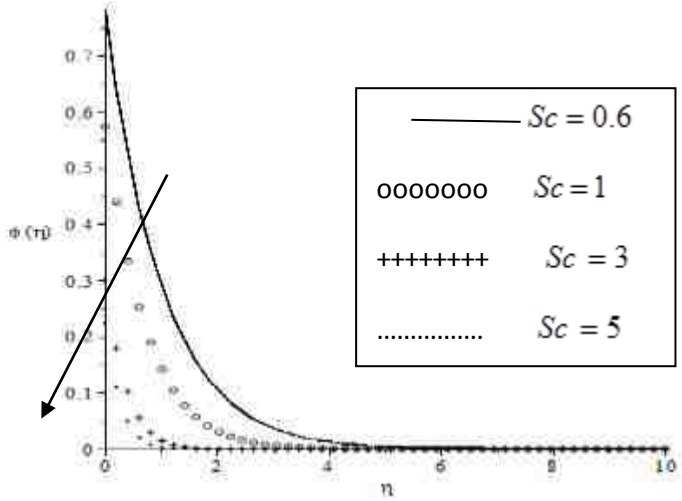

Figure 3.20: Effects of Schmidt number Sc on the concentration profile with fix parameters values of $Gr = Gc = 0.5$, $Sc = 0.6$, $\gamma = 0.2$, $S = M = \lambda = S_v = S_t = S_c = \theta_w = E = 0.1$, $n = 1$, $b = 1$, $Ra = 0.1$, $\Pr = 0.71$, $\lambda = 0.1$

5. Conclusion

This study has investigated the steady-state heat and mass transfer characteristics of Casson fluid flow over an exponentially stretching sheet under prescribed boundary conditions. The model incorporated the effects of viscous dissipation, internal heat generation and an Arrhenius chemical reaction to represent the non-Newtonian, thermally reactive and energy-dissipative nature of such flows. Similarity transformations has made the problem tractable in reducing the governing equations to ordinary differential equations that could be solved numerically. The findings have also demonstrated that velocity, heat and concentration fields are strongly influenced by the Casson parameter, stretching rate and chemical reaction as well as some nonlinear effects noted under high stress. These observations have been discovered useful in the optimization of reactive non-Newtonian fluid processes. Some of the important results are as follows: 1. Yield stress and shear thinning effects take place which are important for industrial and biomedical applications, 2. The heat and concentration boundary layers thicken while fluid motion is suppressed by higher Casson parameters in this process, 3. Heat and mass transfer are improved whereas the momentum boundary layer is thinned by increasing the stretching rate.

References

[1] Ali, F., et al. (2020). Casson fluid model and its applications in biomedical and industrial flows. *Journal of Applied and Computational Mechanics*, 6(3), 1–15.

[2] Asghar, S., et al. (2015). Boundary layer flow over a stretching surface and its industrial applications. *Applied Mathematics and Mechanics*, 36(5), 567–580.

[3] Bég, O. A., et al. (2013). Heat and mass transfer in non-Newtonian flow over stretching sheets with chemical reaction effects. *International Journal of Heat and Mass Transfer*, 62, 97–105.

[4] Bognár, G. (2016). Similarity solutions for boundary layer flows induced by stretching sheets. *Applied Mathematics and Computation*, 272, 868–875.

[5] Bognár, G., & Hriczo, K. (2020). Exact and numerical solutions for non-Newtonian fluid flow over stretching surfaces. *Mathematical Problems in Engineering*, 2020, Article ID 1–10.

[6] Deepthi, K., & Rallabandi, V. P. (2023). Yield stress characteristics of human blood and Casson fluid modeling. *Biomechanics and Modeling in Mechanobiology*, 22(2), 455–468.

[7] Elgendi, S. E., et al. (2024). Rheological behavior of Casson fluids with yield stress effects. *Physics of Fluids*, 36(1), 1–14.

[8] Fatahian, H., et al. (2018). Casson fluid model for blood flow under low shear conditions. *Journal of Biomechanics*, 76, 123–131.

[9] Hussain, S., et al. (2022). Boundary layer flow over stretching sheets: A review of classical and modern approaches. *Alexandria Engineering Journal*, 61(4), 2893–2910.

[10] Khan, M., et al. (2015). Heat transfer analysis in boundary layer flow over stretching sheets. *Applied Thermal Engineering*, 84, 301–310.

[11] Khader, M. M., & Babatin, M. M. (2023). Analytical and numerical study of Casson fluid flow with thermal effects. *Results in Physics*, 49, 1–12.

[12] Magyari, E., & Keller, B. (1999). Heat and mass transfer in the boundary layers on an exponentially stretching continuous surface. *Journal of Physics D: Applied Physics*, 32(5), 577–585.

[13] Mustafa, M., et al. (2013). Boundary layer flow and heat transfer of non-Newtonian fluids over stretching surfaces. *Applied Mathematics and Mechanics*, 34(9), 1113–1124.
[14] Panigrahi, P. K., et al. (2020). Modeling blood flow characteristics using the Casson fluid model. *Biomechanics and Modeling in Mechanobiology*, 19(6), 2145–2158.
[15] Rao, A. S. (2018). Nonlinear stretching sheet problems in fluid mechanics. *Journal of Applied Fluid Mechanics*, 11(2), 457–468.
[16] Sakiadis, B. C. (1961). Boundary-layer behavior on continuous solid surfaces: I. Boundary-layer equations for two-dimensional and axisymmetric flow. *AIChE Journal*, 7(1), 26–28.
[17] Sharada, K., & Shankar, B. (2015). Exponentially stretching sheet with heat transfer effects. *International Journal of Engineering Science*, 89, 1–12.
[18] Shaheen, S., et al. (2019). Magnetohydrodynamic boundary layer flow over stretching surfaces. *Journal of Molecular Liquids*, 287, 110945.
[19] Singh, K., et al. (2019). Casson fluid flow over stretching surfaces with heat and mass transfer. *Thermal Science*, 23(4), 2357–2368.
[20] Veerabhadrappa, B. S., et al. (2020). Heat transfer enhancement in non-Newtonian boundary layer flows. *Heat Transfer Research*, 51(10), 873–889.
[21] Crane, L. J. (1970). Flow past a stretching plate. *Zeitschrift für Angewandte Mathematik und Physik*, 21(4), 645–647.